

Saturated hysteresis loops and conduction mechanisms in Mn-doped BiFeO₃ thin films derived from sol–gel process

Yinjuan Ren · Xiaohong Zhu · Caiyun Zhang ·
Jiliang Zhu · Jianguo Zhu · Dingquan Xiao

Received: 22 October 2014 / Accepted: 6 December 2014 / Published online: 13 December 2014
© Springer Science+Business Media New York 2014

Abstract Mn-doped BiFeO₃ (BFO) thin films with nominal composition of BiFe_{1-x}Mn_xO₃ ($x = 0.00, 0.01, 0.03, 0.05, 0.07$) were deposited on (111)Pt/Ti/SiO₂/Si substrates via a simple sol–gel spin-coating method with rapid thermal annealing process. The BFO films with different Mn dopant contents were well crystallized in the perovskite structure and their overlapped (110) diffraction peaks shifted toward higher angles with the increase in Mn content, indicating a slight distortion in the lattice structure. Improved microstructure with smaller grain size and diminished structural defects can be observed in the films of x around 0.03. X-ray photoelectron spectroscopy analysis confirmed the coexistence of 2+ and 3+ electronic states for Fe element and proper substitution of Mn for Fe can decrease the amount of Fe²⁺ while excess doping results in increasing Fe²⁺ content. The intrinsic ferroelectric polarization was hard to be measured in the pure BFO film due to high leakage contribution, whereas the $x = 0.03, 0.05$ and 0.07 films exhibited well-saturated rectangular shape-like ferroelectric hysteresis loops, and more importantly, perfectly closed hysteresis loops were obtained for the $x = 0.03$ film with a $2Pr$ value of $85.2 \mu\text{C}/\text{cm}^2$. The leakage current density in high electric field region was dramatically decreased by Mn doping, e.g. decreased to $3.3 \times 10^{-4} \text{ A}/\text{cm}^2$ at electric field intensity of $170 \text{ kV}/\text{cm}$ for the $x = 0.03$ film. Detailed leakage current characteristic analysis suggested that the dominant conduction mechanism in the pure BFO film was the space charge limited conduction at medium/high electric fields, which was associated with the space charges originated by

oxygen vacancies; however, the leakage current of the $x = 0.03$ film was dominated by the Schottky mechanism in medium/high electric field region.

1 Introduction

Multiferroic materials with typical magnetoelectric coupling can achieve the accommodation between electric and magnetic order parameters, which provides more degrees of freedom in related device applications, such as ferroelectric memories, magneto-resistive devices, spintronics and magnetic tunnel junctions [1, 2]. Although only a few multiferroic compound systems existed in nature or were synthesized in laboratory, multiferroic materials have been attracting more and more attention from researchers owing to their tantalizing potential applications and interesting physical properties [3–5]. As a representative magnetoelectric multiferroic, BiFeO₃ (BFO) has been systematically investigated in recent years because of its high Curie temperature ($T_C = 850 \text{ }^\circ\text{C}$) and Néel temperature ($T_N = 370 \text{ }^\circ\text{C}$), which make it possible in room temperature use [6]. With the progress in thin film fabrication techniques, epitaxial and polycrystalline BFO thin films have been successfully prepared by pulse laser deposition, sputtering, metal–organic chemical vapor deposition, sol–gel, and so on [7–9]. Despite the abundant research results, the high leakage current density is always one of the biggest problems that hamper the practical applications of BFO films. It is known that a high leakage current density should lead to a low breakdown voltage, making it difficult to obtain well-saturated rectangular shape-like ferroelectric hysteresis loops in BFO thin films [10, 11].

Attempts such as doping and/or adding buffer layer have been made to improve the electrical properties of BiFeO₃

Y. Ren · X. Zhu (✉) · C. Zhang · J. Zhu · J. Zhu · D. Xiao
Department of Materials Science, Sichuan University,
Chengdu 610064, China
e-mail: xhzhu@scu.edu.cn

films [12]. In doping aspect, substitution of transition metal elements for Fe site and substitution of rare earth and alkaline earth metal elements for Bi site have been extensively studied to reduce leakage current, considering that the high leakage current is mainly caused by a large concentration of oxygen vacancies due to the highly volatile nature of Bi and the variable oxidation states of Fe (Fe^{2+} and Fe^{3+}) [13–15]. From defect chemistry theory, aliovalent-ion doping affects the oxidation state of iron element and thus the concentration of oxygen vacancies according to charge compensation [16]. In the study of Qi et al. [17], Ti^{4+} addition notably suppressed the leakage current while doping of Ni^{2+} increased the leakage current density of BFO thin films; therefore, they identified two different leakage mechanisms for Ti^{4+} and Ni^{2+} doping. Mn-doped BFO thin films have been studied by pulse laser deposition, metal organic decomposition, chemical solution deposition and sol–gel, some of which revealed saturated ferroelectric polarization versus electric field (P – E) hysteresis loops yet the others not [18–22]. Among these methods, BFO films with well-saturated P – E hysteresis loops prepared by sol–gel process are more difficult to obtain, and thus are relatively less reported. Sol–gel method is known as a good simple way to synthesize BFO films because of its advantageous characteristics of chemical homogeneity, capability of making large area film and good control of stoichiometry [23, 24]. In this work, the BFO films with different Mn doping contents have been fabricated on technologically desirable (111)Pt/Ti/SiO₂/Si substrates via a simple sol–gel spin-coating method, and their crystallization, morphology and electrical properties have been systematically investigated. Very interestingly, an appropriate Mn doping level enhanced greatly the microstructural and electrical properties of the sol–gel-derived BFO films, thereby promoting the achievement of well-saturated rectangular shape-like ferroelectric hysteresis loops in the Mn-doped BFO thin films.

2 Experimental

Mn-doped BiFeO₃ thin films were synthesized via a simple sol–gel method with rapid thermal annealing on (111)Pt/Ti/SiO₂/Si substrates. Starting materials of bismuth nitrate [$\text{Bi}(\text{NO}_3)_3 \cdot 5\text{H}_2\text{O}$] and iron nitrate [$\text{Fe}(\text{NO}_3)_3 \cdot 9\text{H}_2\text{O}$] were firstly dissolved in the mixed solution of prevailing 2-methoxyethanol and a small amount of acetic acid by magnetic stirring. After stirred for 1 h, when bismuth nitrate and iron nitrate had thoroughly dissolved, a certain amount of manganese (Mn^{3+}) acetate [$\text{C}_6\text{H}_9\text{MnO}_6 \cdot 2\text{H}_2\text{O}$] was added to the mixtures for further stirring. When another 11 h stirring had finished, we finally obtained the stoichiometric solution of $\text{BiFe}_{1-x}\text{Mn}_x\text{O}_3$ ($x = 0.00, 0.01,$

$0.03, 0.05, 0.07$) with a concentration of 0.3 M. In order to compensate for the Bi loss caused by volatilization during annealing process, we weighed $\text{Bi}(\text{NO}_3)_3 \cdot 5\text{H}_2\text{O}$ with 0.05 mol excess, thus the mole ratio of bismuth nitrate and iron nitrate was 1.05:1. The processes described above were carried out in an ambient atmosphere at room temperature.

The as-prepared fresh sol of $\text{BiFe}_{1-x}\text{Mn}_x\text{O}_3$ was spin-coated on the cleaned substrates with a rotation rate of 3,000 rpm for 20 s. Then the wet films were put on the hot plates of 80 °C for 5 min and subsequently 180 °C for 5 min to remove volatile materials. Rapid thermal process was selected to crystallize the $\text{BiFe}_{1-x}\text{Mn}_x\text{O}_3$ films. Referring to the results in our past work, the $\text{BiFe}_{1-x}\text{Mn}_x\text{O}_3$ films were annealed at 715 °C for 90 s with a heating rate of 5 °C/s in air [25]. Every layer was annealed after spin coating and the thickness of single layer was approximately 50 nm. A shadow mask designed by us was used to deposit the top electrodes of 0.00071 cm² on the films surfaces by sputtering. At last, the $\text{BiFe}_{1-x}\text{Mn}_x\text{O}_3$ films with top electrodes were annealed at 300 °C for 10 min to make the electrodes and films get full contact.

The crystallographic studies of the $\text{BiFe}_{1-x}\text{Mn}_x\text{O}_3$ films were performed by using X-ray diffraction (XRD, DX-2700, Dandong, China) operated at 40 kV, 30 mA with Cu K α radiation scanned (2θ value) from 20° to 60°. A field-emission scanning electron microscope (FESEM, JSM-7500F, JEOL, Japan) was utilized to observe the surface and cross section morphologies so as to analyse the microstructure of films. In order to investigate the compositions of the $\text{BiFe}_{1-x}\text{Mn}_x\text{O}_3$ films and the combination states of Fe 2p and Mn 2p electrons, the samples were identified by X-ray photoelectron spectroscopy (XPS, AXIS Ultra DLD, KRATOS, Britain), and the spectrum of Fe was fitted to calculate the quantity ratio of Fe^{2+} and Fe^{3+} . In the aspect of electrical properties studies, an HP 4294A impedance analyzer was adopted to measure the dielectric constant (ϵ_r) and the loss tangent ($\tan\delta$) of the $\text{BiFe}_{1-x}\text{Mn}_x\text{O}_3$ films. The ferroelectric polarization versus electric field (P – E) hysteresis loop and leakage current density were measured using a Radiant ferroelectric test system. All the measurements for the $\text{BiFe}_{1-x}\text{Mn}_x\text{O}_3$ films were carried out at room temperature.

3 Results and discussion

Figure 1 shows the XRD patterns of the $\text{BiFe}_{1-x}\text{Mn}_x\text{O}_3$ ($x = 0.00, 0.01, 0.03, 0.05, 0.07$) thin films annealed at 715 °C in air. For all the films, a small amount of $\text{Bi}_2\text{Fe}_4\text{O}_9$ impurity phase was detected and marked by “*”, as shown in Fig. 1. The slight existence of $\text{Bi}_2\text{Fe}_4\text{O}_9$ was not caused by Mn doping but the high sintering temperature according

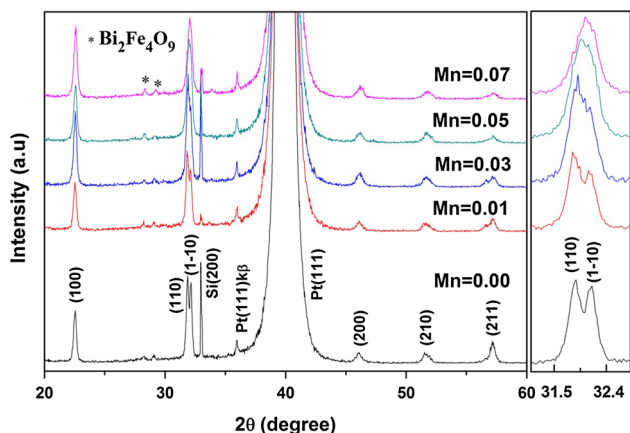


Fig. 1 XRD patterns of BiFe_{1-x}Mn_xO₃ ($x = 0.00, 0.01, 0.03, 0.05, 0.07$) thin films deposited on (111)Pt/Ti/SiO₂/Si substrates with annealing temperature of 715 °C. The right panel shows the magnified patterns in the vicinity of $2\theta = 32^\circ$

to our past work, in which the undoped BiFeO₃ film annealed at 700 °C showed single pure structure while the film annealed at 715 °C possessed little Bi₂Fe₄O₉ impurity phase. It can be deemed that pure BFO will decompose into Bi₂Fe₄O₉ at higher temperature during cooling process. Nonetheless, considering denser microstructure and superior electrical properties for the 715 °C annealed BFO film, we fixed here 715 °C as the target annealing temperature in our Mn-doped BFO experiments. In the magnified patterns of about $2\theta = 32^\circ$ shown on the right side of Fig. 1, reflections of (110) and (1-10) were clearly separated in undoped and $x = 0.01$ films, suggesting that pure and slightly doped BFO films possess perovskite structure with rhombohedral symmetry. With increasing the Mn content, reflection peak (1-10) weakened and overlapped with peak (110). This variation is accompanied with crystalline phase transition, indicating that Mn substitution modified the rhombohedral structure of parental BFO film toward the orthorhombic or tetragonal structure [20, 26]. Besides, the overlapped peak of (1-10) and (110) gradually shifted toward higher angle as the Mn doping content was further increased, which suggests a gradual contraction of the unit cell volume in the film, similar to the report by Palkar et al. [26]. Two possible substitution mechanisms might be considered to explain this phenomenon [27].

- 1 If we assume that iron ions are mainly Fe³⁺, Mn³⁺ is more likely to replace Fe³⁺. Because of the comparable ionic radius for Mn³⁺ ($r(\text{Mn}^{3+}) = 0.645 \text{ \AA}$) and Fe³⁺ ($r(\text{Fe}^{3+}) = 0.645 \text{ \AA}$), Mn³⁺ ↔ Fe³⁺ cannot cause the variation of cell parameters
- 2 Taking into account the conceivable evolution of iron ions as the following equation:



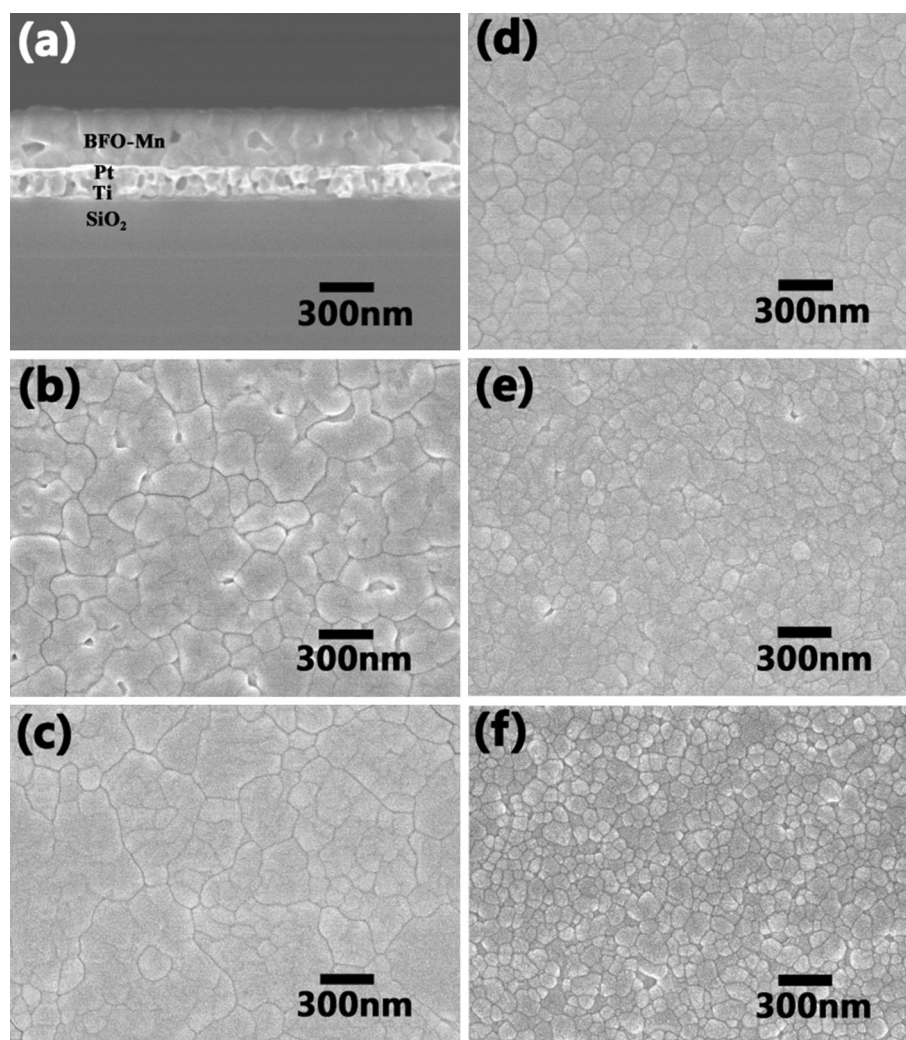
Mn³⁺ ↔ Fe²⁺ might also exist, which could therefore explain the decrease of unit cell volume with the increase in the manganese content, referring to the smaller Mn³⁺ ionic radius in comparison with the larger one of Fe²⁺ ($r(\text{Fe}^{2+}) = 0.78 \text{ \AA}$).

The cross-sectional image of the $x = 0.03$ film and the surface morphology photographs of the $x = 0.00, 0.01, 0.03, 0.05, 0.07$ films detected by FESEM are shown respectively in Fig. 2a, b–f. It is obvious from Fig. 2a that a clear and sharp interface exists between the film and the bottom Pt electrode and they contact well without clear segregation. The thickness of the $x = 0.03$ film is homogeneous with a value of about 300 nm, which is approximately identical for the other Mn-doped films (not shown here). In Fig. 2b, nanosized pores and clear grain boundaries caused by nonuniform growth of grains can be seen for the undoped BFO film. However, the morphologies of the $x = 0.01–0.07$ films are significantly improved by Mn doping, as shown in Fig. 2c–f. In contrast, the Mn-doped BFO films got denser, the grain sizes became smaller, the pores between grains were diminished and the grain boundaries were blurred. On increasing Mn content, the morphologies show that the grain sizes tend to be smaller. It might be understood as: during annealing process, manganese acetate may be decomposed into manganese oxide, and the transient manganese oxides may act as heterogeneous nucleation sites for crystallization [16]. Accordingly, to some extent, under the same annealing conditions, the more nucleation sites exist, the smaller grain sizes will be. To sum up, as can be seen in the images, the films with doping amount around $x = 0.03$ and above show better microstructure.

Figure 3a shows the survey-scan XPS spectrums of the BiFe_{1-x}Mn_xO₃ ($x = 0.00, 0.03, 0.05, 0.07$) thin films. For the $x = 0.03$ film, the photoemission peak of Mn 2p is not obvious and relatively weak compared to the other two doped films because of its less Mn content. For all the films shown in Fig. 3a, apart from stoichiometric elements of Bi, Fe, Mn, O, only C was detected in the scan range of 0–800 eV, which was caused by surface contamination from air and used as criterion to calibrate the binding energy in our XPS measurement. The wide-range XPS spectra confirm the pure element compositions of the BiFe_{1-x}Mn_xO₃ ($x = 0.00, 0.03, 0.05, 0.07$) thin films without any impurities that may be introduced in the experiment process.

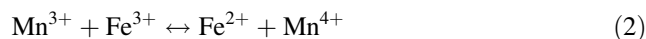
The valence states of Fe ions and their relative contents are closely related to the oxygen vacancy amounts caused by charge compensation effect. The Fe_{Fe³⁺}²⁺ caused by variation of valence states of Fe ions can trap mobile oxygen vacancies and generate defect complexes of $(V_{\text{O}^{2-}})^{\cdot\cdot} - (\text{Fe}_{\text{Fe}^{3+}}^{2+})'$, which play an important role in the dielectric and ferroelectric properties

Fig. 2 FESEM images of $\text{BiFe}_{1-x}\text{Mn}_x\text{O}_3$ ($x = 0.00, 0.01, 0.03, 0.05, 0.07$) thin films: **a** cross-section image of $x = 0.03$ film, **b–f** surface morphologies of $x = 0.00, 0.01, 0.03, 0.05, 0.07$ films



of the $\text{BiFe}_{1-x}\text{Mn}_x\text{O}_3$ thin films [28]. Accordingly, it is very necessary to study the narrow-scan XPS spectra of Fe 2p, as shown in Fig. 3b, to get the valence information for further electrical properties analysis. From the core level XPS spectra of Fe 2p, it is visible that the usual two main peaks of $2p_{3/2}$ and $2p_{1/2}$ arising from spin–orbital interaction appear for the $x = 0.00, 0.03, 0.07$ thin films. Besides, satellite peaks were also detected, which were ascribed to different d orbital electron configurations for Fe^{2+} and Fe^{3+} , resulting in the different satellite peaks positions from $2p_{3/2}$ main peaks [29]. The Fe $2p_{3/2}$ asymmetric peaks of these three samples with different doping amounts were fitted by using the XPS Peak software with the function GL(20) [GL(p)—product of Gaussian(0)–Lorentzian(100)] and Shirley background subtraction. The fitting results delineated in Fig. 3b confirm the coexistence of Fe^{3+} and Fe^{2+} in our films. The concentration ratios of Fe^{2+} to all Fe ions were calculated from the fitted peak areas and given as 33.5, 26.8, 39.5 % for the $x = 0.00, 0.03, 0.07$ films, respectively. Hence, the $x = 0.03$ film

possesses the least amount of Fe^{2+} ions among the three films while the undoped BFO film has fewer Fe^{2+} ions than the $x = 0.07$ film. Without Mn doping, BFO film possesses Fe^{3+} and Fe^{2+} ions because of the conversion of Fe^{3+} to Fe^{2+} ions accompanied by the generation of oxygen vacancies to keep local charge neutrality. After introducing Mn^{3+} into the perovskite network, Fe^{3+} and Fe^{2+} are replaced by Mn^{3+} , so that the detected amount of Fe^{2+} in the $x = 0.03$ film is lower than that in pure BFO film. As reported by Ianculescu [27], for the substitution of Fe^{3+} by Mn^{3+} , a few Fe^{3+} ions are converted into Fe^{2+} on the expense of the oxidation of some Mn^{3+} ions, which could be described as follows:



Since the increase in iron ionic radius from 0.645 \AA (Fe^{3+}) to 0.78 \AA (Fe^{2+}) is accompanied by a decreased manganese ionic radius from 0.645 \AA (Mn^{3+}) to 0.53 \AA (Mn^{4+}), the unit cell volume is likely to keep the same, and therefore, it is not the reason for the observed decrease in

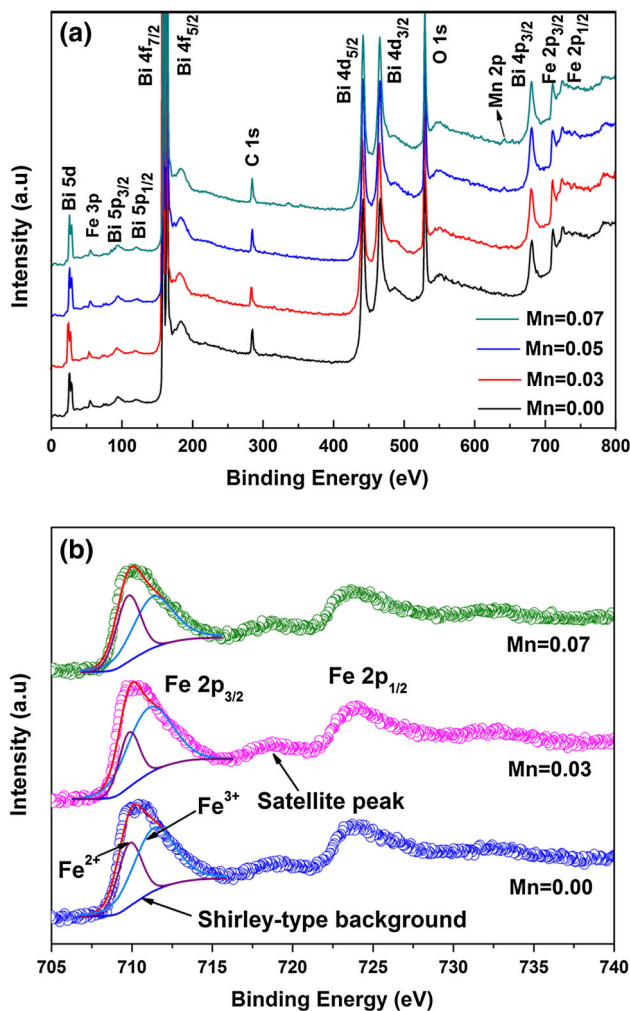


Fig. 3 **a** XPS survey spectra of $\text{BiFe}_{1-x}\text{Mn}_x\text{O}_3$ ($x = 0.00, 0.03, 0.05, 0.07$) thin films, **b** the fitted narrow-scan spectra of Fe 2p for $x = 0.00, 0.03, 0.07$ films

unit cell volume for the doped films. Nonetheless, with further increase in the amount of Mn, the redox reaction shown above becomes more pronounced, thereby resulting in more Fe^{2+} formed in the film. Hence, more Fe^{2+} ions were detected in the $x = 0.07$ film. Then we can conclude that the $x = 0.03$ film has the fewest defect pairs of $(V_{\text{O}^{2-}})^{\cdot\cdot} - (\text{Fe}_{\text{Fe}^{3+}}^{2+})^{\cdot}$ compared to the other two films. It should be noted that because of the slight amount of Mn, it is difficult to obtain reliable and robust quantitative results from the XPS spectra of Mn.

Figure 4 displays the dielectric properties of the $\text{BiFe}_{1-x}\text{Mn}_x\text{O}_3$ ($x = 0.00, 0.01, 0.03, 0.05, 0.07$) films in the measured frequency range from 1 kHz to 1 MHz at room temperature. As shown in Fig. 4a, for all the films, the dielectric permittivity (ϵ_r) exhibits maximum values at the lowest test frequency of 1 kHz, which monotonously

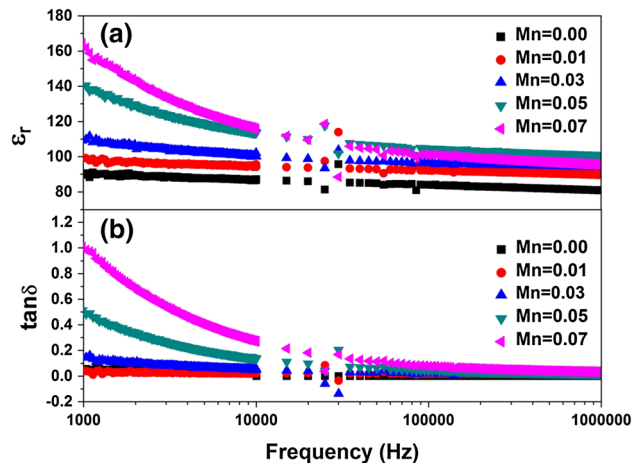


Fig. 4 **a** Relative dielectric constant and **b** dielectric loss tangent of $\text{BiFe}_{1-x}\text{Mn}_x\text{O}_3$ ($x = 0.00, 0.01, 0.03, 0.05, 0.07$) thin films as a function of the measurement frequency

increases with increasing the Mn concentration. The low doped samples show better frequency-independent response, whereas for the $x = 0.05$ and 0.07 doped films, ϵ_r decreases rapidly with increasing the frequency in low test range. This phenomenon can be attributed to the dominant influence factors of dipole orientation polarization and interfacial polarization. At low frequencies, defect complexes of $(V_{\text{O}^{2-}})^{\cdot\cdot} - (\text{Fe}_{\text{Fe}^{3+}}^{2+})^{\cdot}$ can align along the direction of the applied electric field to increase the dielectric constant, but at high frequencies, those dipoles are unable to be in step with the frequency, resulting in dielectric relaxation [30]. Consequently, the $x = 0.07$ sample exhibiting the most Fe^{2+} and oxygen vacancies from the XPS analysis has the highest ϵ_r and dramatic dielectric relaxation process in low frequency region. The ϵ_r value for the $x = 0.03$ film is higher than that of the undoped film though it possesses fewer Fe^{2+} ions, and that may be due to the denser microstructure in the $x = 0.03$ film.

The dielectric loss ($\tan\delta$) shows the same trend as ϵ_r with increasing the Mn doping quantities in low frequency region, as indicated in Fig. 4b, whereas they become difficult to discriminate with low values in high frequency region for all the compositions. Not only the relaxation loss, which is associated with dipoles, but also the resistive loss, which is rather related to leakage current density, dominates the $\tan\delta$ of films [31]. The composition $x = 0.03$ has the lowest leakage current density as will be discussed below; meanwhile, it possesses the fewest defect complexes of $(V_{\text{O}^{2-}})^{\cdot\cdot} - (\text{Fe}_{\text{Fe}^{3+}}^{2+})^{\cdot}$, so the better $\tan\delta$ response for $x = 0.03$ becomes reasonable when compared to the other degrees of Mn addition.

Figure 5a shows the room temperature P - E hysteresis loops of the $\text{BiFe}_{1-x}\text{Mn}_x\text{O}_3$ ($x = 0.00, 0.01, 0.03, 0.05,$

0.07) thin films measured at the frequency of 2 kHz. The $x = 0.03, 0.05$ and 0.07 films show well-saturated rectangular shape-like P – E loops with $2P_r$ values of $84.2 \mu\text{C}/\text{cm}^2$, 79.5 and $93.8 \mu\text{C}/\text{cm}^2$, respectively. The highest remanent polarization (P_r) value for the $x = 0.07$ film may be due to its poorest rectangularity and largest leakage current density compared to the $x = 0.03$ and 0.05 films. Thanks to the lower leakage current and denser microstructure, the $x = 0.03$ film exhibits more closed loop and better voltage tolerance of $1,223 \text{ kV}/\text{cm}$ than the $x = 0.05$ film with $1,025 \text{ kV}/\text{cm}$. By contrast to the $x = 0.03$ and 0.05 films, the film $x = 0.07$ displays the highest coercive field that shows great respect to its maximum oxygen vacancies (referring to the XPS results). This phenomenon can be comprehended as: during the aging process, defect complexes of $(V_{O^{2-}})^{\cdot\cdot} - (\text{Fe}_{\text{Fe}^{3+}}^{2+})'$ may align along the direction of spontaneous polarization, and these aligned defect complexes could provide a force to block the domain switching [32, 33]. Therefore, a higher applied field would

be needed to switch the ferroelectric domains in the $x = 0.07$ film. The hysteresis loops for the $x = 0.00$ and 0.01 compositions are unsaturated, especially for the $x = 0.00$ sample (see the inset of Fig. 5a), which shows a lossy loop behavior caused by vast charge defects and porous microstructure, and that could induce low breakdown voltage. As proved, the better P – E loops for the Mn-doped films may also be linked to the increase of tetragonality in the crystal structure verified in XRD analysis. The increased tetragonality can boost the ferroelectricity in the Mn-doped BFO films propounded by Ederer and Spaldin [34]. In addition, the ferroelectric properties of the BFO films can be dramatically improved by the addition of Mn because of decreased oxygen-related defects and improved breakdown voltage and microstructure. The evolution of the ferroelectric loop for the $x = 0.03$ film measured at 2 kHz with various voltages is illustrated in Fig. 5b. As shown in the figure, the $x = 0.03$ film exhibits good intrinsic ferroelectricity without any noticeable leakage current contribution.

In order to investigate the conduction mechanisms involved in leakage behavior of the different degrees doped BFO films, I – V curves were measured with both polarities of the applied voltages at room temperature. Figure 6a shows the logarithmic plot of the leakage current density J versus applied field E relations. It can be seen that the $x = 0.03$ film exhibits the most superior leakage characteristic with a low J value of $3.3 \times 10^{-4} \text{ A}/\text{cm}^2$ at $E = 170 \text{ kV}/\text{cm}$ compared to $2.7 \times 10^{-3} \text{ A}/\text{cm}^2$ for the film $x = 0.05$ and $9.0 \times 10^{-3} \text{ A}/\text{cm}^2$ for the film $x = 0.07$ at the same electric field. As discussed above, the film $x = 0.07$ has more oxygen vacancies, which can serve as the trapping centers for electrons, thereby increasing the leakage current [35], so it is reasonable for the higher current density in the $x = 0.07$ film than that in the $x = 0.03$ film. From Fig. 6a, we can also find that the dependences of leakage current on electric field for the $x = 0.03$ – 0.07 films are different from the $x = 0.00$ and 0.01 films, because the latter ones reveal a faster increase trend. We ascribe the difference in leakage current increasing trend to their different conduction mechanisms that are going to be discussed below. Consequently, Mn doping not only decreases the leakage current density in BFO film, but also changes its conduction mechanism.

For undoped BFO film, $\log(J)$ versus $\log(E)$ curve under positive bias is plotted in Fig. 6b. As shown in the figure, the leakage current can be well fitted by a straight line with a slope of 2.0 in the middle and high field region, indicating a power law relationship $J \propto E^2$. Thus the space charge limited conduction (SCLC) is predominant in pure BFO film according to Qi et al. [17]. Based on the work of Scott et al. [36], in many ferroelectric materials, oxygen vacancy is the primary reason to originate space charge for SCLC

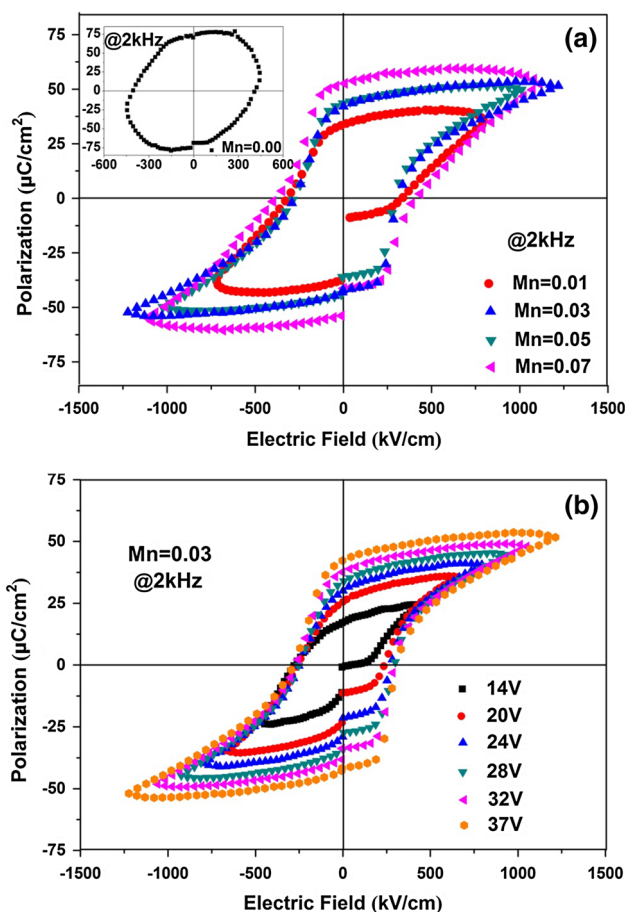


Fig. 5 **a** Room temperature ferroelectric hysteresis loops of $\text{BiFe}_{1-x}\text{Mn}_x\text{O}_3$ ($x = 0.01, 0.03, 0.05, 0.07$) thin films, with the inset showing that of $x = 0.00$ film. **b** Ferroelectric hysteresis loops for $x = 0.03$ film measured at 2 kHz with various voltages

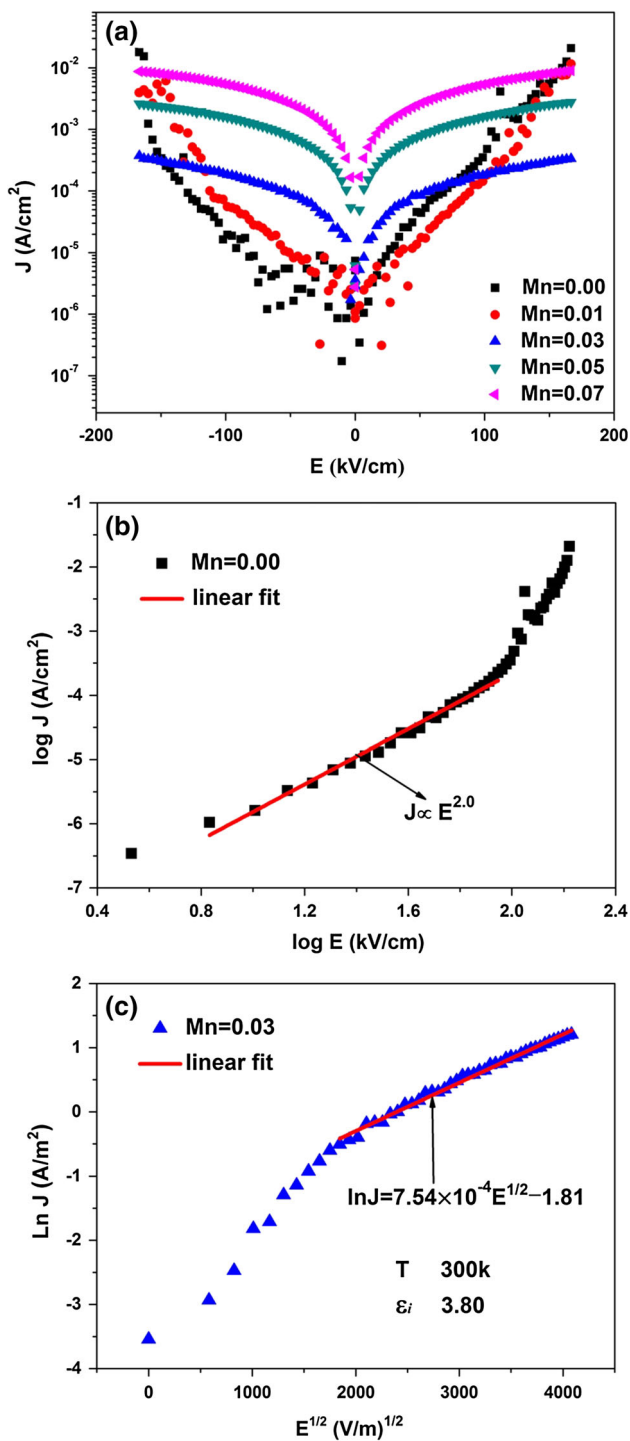


Fig. 6 **a** Leakage current density of $\text{BiFe}_{1-x}\text{Mn}_x\text{O}_3$ ($x = 0.00, 0.01, 0.03, 0.05, 0.07$) thin films. **b** $\log(J)$ versus $\log(E)$ curve for $x = 0.00$ film and **c** $\ln(J)$ versus $E^{1/2}$ plot for $x = 0.03$ film in positive bias voltages

mechanism, so the leakage current in pure BFO film is mainly caused by its abundant oxygen vacancies in the middle and high field region. And at low electric fields, just like many reported results, the leakage current is subject to Ohmic mechanism (not shown here).

Considering the fewer oxygen vacancies in the $x = 0.03$ film compared to pure BFO film, we firstly exclude the SCLC mechanism for the $x = 0.03$ film. After testing several possible conduction mechanisms, we found that Schottky mechanism can well explain the leakage current in the $x = 0.03$ film. Schottky equation is given by [37]:

$$J = A * T^2 \exp \left[\frac{-q(\phi_b - \sqrt{qE/4\pi\epsilon_i\epsilon_0})}{kT} \right] \tag{3}$$

where J is the current density, A^* is the effective Richardson coefficient, T is the absolute temperature, q is the charge of electron, ϕ_b is the Schottky barrier height, E is the applied electric field, ϵ_i is the optical frequency dielectric constant, ϵ_0 is the permittivity of free space, and k is the Boltzmann constant. It should be noted that the plot of $\ln(J)$ versus $E^{1/2}$ exhibits a linear relation for the Schottky mechanism, and the optical frequency dielectric constant ϵ_i can be calculated utilizing the slope of the fitting line. Figure 6c shows the $\ln(J)$ versus $E^{1/2}$ plot for the $x = 0.03$ film in positive bias voltages. The plot can be well fitted in a straight line with the equation of $\ln J = 7.54 \times 10^{-4} E^{1/2} - 1.81$ in the middle and high field region. With the slope value of 7.54×10^{-4} and T of 300 K, we finally obtained the ϵ_i of 3.797. As the refraction index (n) for BFO is commonly determined to be about 2.5, and Sharma et al. [38] reported 2.21 in their $\text{BiFe}_{0.9}\text{Mn}_{0.1}\text{O}_3$ thin film, the ϵ_i for the Mn-doped BFO films should be similar in the low single-digit range via the equation of $\epsilon_i = n^2$ [39]. Regarding the ϵ_i of 3.797 for the $x = 0.03$ film, the Pt/ $\text{BiFe}_{0.97}\text{Mn}_{0.03}\text{O}_3$ interface conduction current can be well described by the Schottky equation in the middle and high field region. It is worth noting that Ohmic mechanism can also explain the leakage current of the doped BFO film in low electric field region (not shown here).

4 Conclusions

Polycrystalline $\text{BiFe}_{1-x}\text{Mn}_x\text{O}_3$ ($x = 0.00, 0.01, 0.03, 0.05, 0.07$) thin films were successfully synthesized using a simple sol-gel spin-coating process on (111)Pt/Ti/SiO₂/Si substrates. After introducing Mn into the BFO lattice, a slight lattice distortion was identified by XRD with overlapped (110) peak shifting toward higher angle. The microstructure of BFO films was significantly improved by Mn doping, and the $\text{BiFe}_{1-x}\text{Mn}_x\text{O}_3$ film possessed the best compactness when $x = 0.03$. XPS analysis revealed that Fe ions existed in 2+ and 3+ electronic states. Moreover, $x = 0.03$ Mn doping availably suppressed the origination of oxygen vacancies though higher Mn addition contents might increase oxygen vacancies. Also, Mn doping can

raise dielectric permittivity and keep dielectric loss low at the same time. For the $x = 0.05$ and 0.07 doped films, their relatively high dielectric constant and dielectric loss in low frequency region were ascribed to the defect complexes of $(V_{O^{2-}})^{\cdot\cdot} - (Fe_{Fe^{3+}}^{2+})^{\cdot}$ associated with high oxygen vacancy concentrations. Well-saturated rectangular shape-like P – E loops were obtained for the $x = 0.03$, 0.05 and 0.07 films, especially for the $x = 0.03$ film, closed excellent hysteresis loop proved the good intrinsic ferroelectricity in the film. The leakage current of BFO films was dramatically decreased by $x = 0.03$ Mn doping. At medium/high electric fields, SCLC and Schottky mechanisms dominate the leakage current of pure BFO and $x = 0.03$ Mn-doped BFO films, respectively.

Acknowledgments This work was supported by the National Natural Science Foundation of China (Grant No. 61071017), the Programme for New Century Excellent Talents in University of China (Grant No. NCET-10-0582), the Doctoral Fund of the Ministry of Education of China (Grant No. 20100181120021) and the Programme for Outstanding Young Scientific and Technological Leaders of Sichuan Province, China (Grant No. 2011JQ0021).

References

- R. Ramesh, N.A. Spaldin, *Nat. Mater.* **6**, 21 (2007)
- N.A. Hill, *J. Phys. Chem. B* **104**, 6694 (2000)
- R. Seshadri, N.A. Hill, *Chem. Mater.* **13**, 2892 (2001)
- W. Eerenstein, N.D. Mathur, J.F. Scott, *Nature* **442**, 759 (2006)
- M. Fiebig, *J. Phys. D Appl. Phys.* **38**, R123–R152 (2005)
- J. Wang, J.B. Neaton, H. Zheng, V. Nagarajan, S.B. Ogale, B. Liu, D. Viehland, V. Vaithyanathan, D.G. Schlom, U.V. Waghmare, N.A. Spaldin, K.M. Rabe, M. Wutting, R. Ramesh, *Science* **299**, 1719 (2003)
- J. Li, J. Wang, M. Wuttig, R. Ramesh, N. Wang, B. Ruetter, A.P. Pyatakov, A.K. Zvezdin, D. Viehland, *Appl. Phys. Lett.* **84**, 5261 (2004)
- R.Y. Zheng, X.S. Gao, Z.H. Zhou, J. Wang, *J. Appl. Phys.* **101**, 054104 (2007)
- S.Y. Yang, F. Zavaliche, L. Mohaddes-Ardabili, V. Vaithyanathan, D.G. Schlom, Y.J. Lee, Y.H. Chu, M.P. Cruz, Q. Zhan, T. Zhao, R. Ramesh, *Appl. Phys. Lett.* **87**, 102903 (2005)
- Y.P. Wang, L. Zhou, M.F. Zhang, X.Y. Chen, J.M. Liu, Z.G. Liu, *Appl. Phys. Lett.* **84**, 1731 (2004)
- J.R. Cheng, L.E. Cross, *J. Appl. Phys.* **94**, 5188 (2003)
- Y. Wang, C.W. Nan, *Thin Solid Films* **517**, 4484 (2009)
- T. Kawae, Y. Terauchi, H. Tsuda, M. Kumeda, A. Morimoto, *Appl. Phys. Lett.* **94**, 112904 (2009)
- Z.Q. Hu, M.Y. Li, B.F. Yu, L. Pei, J. Liu, J. Wang, X.Z. Zhao, *J. Phys. D Appl. Phys.* **42**, 185010 (2009)
- L.H. Yin, W.H. Song, X.L. Jiao, W.B. Wu, X.B. Zhu, Z.R. Yang, J.M. Dai, R.L. Zhang, Y.P. Sun, *J. Phys. D Appl. Phys.* **42**, 205402 (2009)
- C.F. Chung, J.P. Lin, J.M. Wu, *Appl. Phys. Lett.* **88**, 242909 (2006)
- X.D. Qi, D. Joonghoe, T. Rumen, G.B. Mark, L.M.D. Judith, *Appl. Phys. Lett.* **86**, 062903 (2005)
- X.H. Zhu, H. Béa, M. Bibes, S. Fusil, K. Bouzehouane, E. Jacquet, A. Barthélémy, D. Lebeugle, M. Viret, D. Colson, *Appl. Phys. Lett.* **93**, 082902 (2008)
- Z. Wen, G.D. Hu, S.H. Fan, C.H. Yang, W.B. Wu, Y. Zhou, X.M. Chen, S.G. Cui, *Thin Solid Films* **517**, 4497 (2009)
- S.K. Singh, H. Ishiwaru, K. Sato, K. Maruyama, *J. Appl. Phys.* **102**, 094109 (2007)
- W.L. Liu, G.Q. Tan, G.H. Dong, X. Yan, W. Ye, H.J. Ren, A. Xia, *J. Mater. Sci.: Mater. Electron.* **25**, 723 (2014)
- M. Sahni, N. Kumar, S. Singh, A. Jha, S. Chaubey, M. Kumar, M.K. Sharma, *J. Mater. Sci.: Mater. Electron.* **25**, 2199 (2014)
- Y. Wang, Q.H. Jiang, H.C. He et al., *Appl. Phys. Lett.* **88**, 142503 (2006)
- H.R. Liu, Z.L. Liu, Q. Liu, K.L. Yao, *Thin Solid Films* **500**, 105 (2006)
- Y.J. Ren, X.H. Zhu, C.Y. Zhang, J.L. Zhu, J.G. Zhu, D.Q. Xiao, *Ceram. Int.* **40**, 2489 (2014)
- V.R. Palkar, D.C. Kundaliya, S.K. Malik, *J. Appl. Phys.* **93**, 4337 (2003)
- A. Ianculescu, F.P. Gheorghiu, P. Postolache, O. Oprea, L. Mitoseriu, *J. Alloys Compd.* **504**, 420 (2010)
- Z. Wen, G. Hu, C. Yang, W. Wu, *Appl. Phys. A* **97**, 937 (2009)
- L. Bi, A.R. Taussig, H.S. Kim, L. Wang, G.F. Dionne, D. Bono, K. Persson, G. Ceder, C.A. Ross, *Phys. Rev. B* **78**, 104 (2008)
- W.J. Jie, J. Zhou, W.F. Qin, X.H. Wei, J. Xiong, Y. Zhang, A. Bhalla, Y.R. Li, *J. Phys. D Appl. Phys.* **40**, 2854 (2007)
- M. Nayak, S.Y. Lee, T.Y. Tseng, *Mater. Chem. Phys.* **77**, 34 (2002)
- L. Zhang, X. Ren, *Phys. Rev. B* **73**, 094121 (2006)
- G.D. Hu, S.H. Fan, C.H. Yang, W.B. Wu, *Appl. Phys. Lett.* **92**, 192905 (2008)
- C. Ederer, N.A. Spaldin, *Phys. Rev. Lett.* **95**, 257601 (2005)
- Z.M. Yin, J.J. Liu, G.D. Hu, W.B. Wu, C.H. Yang, *J. Alloys Compd.* **509**, 3766 (2011)
- J.F. Scott, C.A. Araujo, B.M. Melnick, L.D. McMillan, R. Zuleeg, *J. Appl. Phys.* **70**, 382 (1991)
- S.M. Sze, *Physics of Semiconductor Devices*, 2nd edn. (Wiley, New York, 1981)
- H.B. Sharma, N. Boinis Singh, K. Nomita Devi, J.H. Lee, S. Bobby Singh, *J. Alloys Compd.* **583**, 106 (2014)
- S. Iakovlev, C.H. Solterbeck, M. Kuhnke, M. Es-Souni, *J. Appl. Phys.* **97**, 094901 (2005)